

Article

Preparation of Zeolitic Imidazolate Framework and Carbon Nanofiber Composites for Nitrofurazone Detection

Haobo Wang^{1,2}, Subramanian Sakthinathan^{1,2}, Arjunan Karthi Keyan^{1,2}, Chung-Lun Yu^{1,2}, Satoshi Kameoka³, Te-Wei Chiu^{1,2,*}  and Karuppiyah Nagaraj⁴

¹ Department of Materials and Mineral Resources Engineering, National Taipei University of Technology, No. 1, Section 3, Zhongxiao East Road, Taipei 106, Taiwan; t109789402@ntut.edu.tw (H.W.); sakthinathan@ntut.edu.tw (S.S.); t108a09417@ntut.edu.tw (A.K.K.); 109789003@ntut.org.tw (C.-L.Y.)

² Institute of Materials Science and Engineering, National Taipei University of Technology, No. 1, Section 3, Chung-Hsiao East Road, Taipei 106, Taiwan

³ Institute of Multidisciplinary Research for Advanced Materials, Tohoku University, Katahira 2-1-1, Sendai 980-8577, Japan; satoshi.kameoka.b4@tohoku.ac.jp

⁴ School of Pharmacy, National Forensic Sciences University, 6M56+XP8, Police Bhavan Road, Sector 9, Gandhinagar 382007, India; k.nagaraj@nfsu.ac.in

* Correspondence: tewei@ntut.edu.tw (T.W.C.)

Abstract: Metal–organic frame (MOF) materials may have the advantages of a regular pore structure, large porosity, and large specific surface area, which could provide better catalytic activity, but they have some disadvantages in electrocatalysis. In contrast, carbon nanofibers (CNFs) prepared by electrospinning methods have good conductivity and stability. Therefore, this research aimed to generate MOF/CNFs composite materials to improve the electrochemical properties of MOF materials and apply them to the field of electrochemical sensing. This experiment was based on the preparation of straight unidirectional CNFs by an electrospinning method at 2000 RPM. The original method of preparing zeolitic imidazolate frameworks (ZIF-8) was improved and ZIF-8 was uniformly dispersed on the surface of CNFs to form a ZIF-8/CNF composite with a fiber diameter of about 0.10 to 0.35 μm . The specific surface area of the CNFs was about 42.28 m^2/g , while that of the ZIF-8/CNF composite was about 999.82 m^2/g . The specific surface area of the ZIF-8/CNF composite was significantly larger than that of CNFs. The GCE/ZIF-8/CNF electrode had an excellent electrochemical reaction, with an oxidation peak at about 216 μA , which proved that the ZIF-8/CNF composite material would have good catalytic activity and excellent electrochemical properties for the detection of nitrofurazone compared to other modified electrodes.

Keywords: electrospinning; ZIF-8; carbon nanofibers; MOF material; nitrofurazone; real sample analysis



Citation: Wang, H.; Sakthinathan, S.; Keyan, A.K.; Yu, C.-L.; Kameoka, S.; Chiu, T.-W.; Nagaraj, K. Preparation of Zeolitic Imidazolate Framework and Carbon Nanofiber Composites for Nitrofurazone Detection. *Micro* **2024**, *4*, 14–32. <https://doi.org/10.3390/micro4010002>

Academic Editor: Nurettin Sahiner

Received: 2 November 2023

Revised: 3 January 2024

Accepted: 4 January 2024

Published: 9 January 2024



Copyright: © 2024 by the authors. Licensee MDPI, Basel, Switzerland. This article is an open access article distributed under the terms and conditions of the Creative Commons Attribution (CC BY) license (<https://creativecommons.org/licenses/by/4.0/>).

1. Introduction

Nitrofurazone (5-nitro-2-furaldehyde semicarbazone) is a synthetic antibiotic medicine that has been widely utilized to treat bacterial and protozoan infections. Nitrofurazone (NFZ) is used to treat both humans and animals for inflammatory illnesses, as well as Gram-positive and Gram-negative bacterial diseases of the skin, genitourinary tract, eyes, nose, and ears. However, nitrofurazone drug residues may enter the ecosystem, food chain, and drinking water. Long-term intake of this antibiotic can lead to liver disease, lung fibrosis, carcinogenicity, and birth defects [1,2]. Because of its dangers, the use of this antibiotic is prohibited for both people and animals in many nations, including the European Union. Nevertheless, due to its low cost and excellent antibacterial effectiveness, it is still used illegally in many countries [3]. Hence, it is crucial to detect NFZ in food and drink and to remove it from water, soil, and food. A few techniques that have been used to detect NFZ are high-performance liquid chromatography, liquid chromatography–mass spectrometry, spectrophotometry, and electrochemical detection. The electrochemical sensor is suitable

for the on-site examination of targets due to its favorable characteristics, such as simplicity, portability, and quick reaction [4,5].

In the past three decades, porous materials have attracted great attention in many fields of exploration, including physics, chemistry, and materials science [6–8]. These materials play significant roles in our daily activities, with a wide range of applications such as adsorption, separation, biomedicine, and catalysis. Metal–organic frameworks (MOFs), also known as porous coordination polymers (PCPs), are constructed of organic linkers and metal ions or clusters, and they have emerged as a new type of crystalline material with a large surface area (typically ranging from 1000 to 10,000 m²/g), high porosity, tunable structures, and flexible tailoring ability compared with traditional porous materials such as zeolites [9–11]. MOFs can cover the full pore size gap between microporous zeolites and mesoporous silica structures and have highly tunable pore sizes (usually 0–3 nm; up to 9.8 nm). MOFs have a diverse range of applications, including gas absorption, separation, chemical sensors, biomedicine, proton conductivity, and heterogeneous catalysis [12–15].

The reason for the wide interest in MOFs is their well-defined and tailorable crystalline structures, which make them an ideal platform for the establishment of clear structure and property relationships. These structures and properties have great significance and provide more guidelines for the design of new functional materials [16]. In 2015, Chen Jun et al. synthesized Ni-MOFs by a solvothermal method as a high-performance rechargeable lithium-oxygen battery cathode catalyst. The test results showed that the specific capacity of Ni-MOFs was 9000 mAh/g [17]. In 2020, Hu Ning et al. used MOF-assisted ruthenium atoms with nitrogen-containing porous carbon (Ru SAs-NC) for supercapacitors and reported a current density of 0.02 mA cm⁻² [18].

Zeolitic imidazolate frameworks (ZIFs) are porous hybrid materials with structures analogous to zeolites that are connected with four tetrahedral units, wherein metal ions, such as Zn²⁺ or Co²⁺, are linked through N atoms in ditopic imidazolate anions [19,20]. ZIFs have high pore sizes, surface functionality, and relatively high chemical and thermal stability. They have emerged as a potential material for H₂ storage [21], CO₂ adsorption [22], alkane/alkene separation [23], and heterogeneous catalysis [24], owing to their structural properties [25]. In 2015, Jiang Hailong et al. combined the high catalytic activity of ZIF-8 and ZIF-67, each with high specific surface areas, and used element doping to replace Zn with Co to obtain a high-specific-surface-area catalyst with excellent ORR catalytic activity [26]. In 2017, L. J. Feng et al. and others obtained a series of zinc-doped cobalt (ZnCoNC) that provides good conductivity for the composite material and shows excellent ORR and OER catalytic activity [27].

In 1991, Iijima et al. discovered and reported carbon nanofibers (CNFs), which have received extensive attention in electrochemical studies [28]. CNF materials are formed by crimping multiple layers of graphite sheets. The fiber diameters are generally 10–500 nm, and their lengths are about 0.5–100 μm. In addition, CNFs have not only good electrical conductivity but also high mechanical strength, a large aspect ratio, a large specific surface area, and good thermal stability. These properties make CNFs useful in a wide range of applications in the fields of electrode materials, sensors, reinforcement materials, catalysts, nano-photoelectric materials, heavy metal ion adsorption, and hydrogen storage [29–31].

Many materials can be used as a carbon source for CNF preparation, including polyacrylonitrile (PAN), polyvinyl alcohol (PVA), polyimide (PI), and polyvinylidene fluoride (PVDF) [32]. However, when polyacrylonitrile is used as the carbon source, a low-temperature stabilization process must be applied during the heat treatment to keep the fiber morphology and structure of CNFs stable. The preparation of CNFs using polyacrylonitrile as a carbon source was first proposed by Kim et al. [33]. At present, there are many methods for preparing carbon nanofibers, but most of them are still at the laboratory level. Because CNFs have very broad application prospects, the industrial production of CNFs will soon be necessary [34,35].

The current methods for preparing CNFs include chemical vapor deposition, and solid-phase synthesis [36,37]. These methods have problems such as high production costs, low

production efficiency, and complicated production processes. At present, electrospinning is the most commonly used method of nano- and microfiber preparation. It can directly prepare polymer nanofibers. Compared with other methods, electrospinning is a relatively simple, and fast method of preparing nanofiber, and it has great application potential in the fields of biomedicine, filtration, sensors, catalysis, and energy storage [38–41].

Electrospinning was first patented in the United States in 1902, but it was not revisited until the 1990s [42]. Currently, electrospinning is a low-cost method that can produce nanofibers, and it can be used to make not only core-shell or hollow fibers but also a range, from single fibers to ordered fibers [43–45]. Electrospinning is an electrohydrodynamic process based on inducing the density of electrostatic charges on the molecules of the solution so that the self-repulsion of the charges causes the liquid to stretch into fibers in an electric field. In the electrospinning process, the applied voltage, flow rate, humidity, and temperature are important factors [46].

Electrospinning methods are very useful for the development of various structures whose functions depend on the surface area. This method can produce fibers with diameters in the millimeter (mm) to nanometer (nm) range. In energy and environmental applications, electrospun nanofibers have been used in electronics, sensor technology, catalysis, filtration, medical solar cells, lithium-ion batteries, fuel cells, hydrogen storage, and supercapacitors [47–52].

In this work, we describe the preparation of a ZIF-8/CNF composite by a flexible and simple method and characterization studies of the material. The prepared composite was examined in scanning electron microscope (SEM), X-ray diffraction analysis (XRD), Transmission Electron Microscopy (TEM), Raman spectroscopy, and Brunauer–Emmett–Teller (BET) studies. Electrochemical properties of the GCE/ZIF-8/CNF₅ electrode were examined in Electrochemical Impedance spectroscopy (EIS), Cyclic Voltammetry (CV), and Differential pulse voltammetry (DPV) studies. The ZIF-8/CNF composite was applied for NFZ detection and shown to have excellent electrochemical activity for real sample analysis. The prepared GCE/ZIF-8/CNF electrode demonstrated high sensitivity and selectivity and the lowest detection limit for NFZ detection. At the same time, this detection technique still has some drawbacks, such as costly raw materials, environmental pollution during the electrode preparation, and a long preparation time.

2. Materials and Methods

Polyacrylonitrile (PAN) (C₃H₃N; Molecular mass: 150,000 g/mol; Purity: 99.0%), zinc nitrate hexahydrate (Zn(NO₃)₂·6(H₂O); Molecular mass: 297.49 g/mol; Purity: 99%), and 2-methylimidazole (C₄H₆N₂; Molecular mass: 82.1 g/mol; Purity: 99%) were obtained from Sigma-Aldrich chemical company, Taiwan. N, N-Dimethylformamide (DMF) (C₃H₇NO; Molecular mass: 73.09 g/mol; Purity: 99.5%) was obtained from Tedia Chemical Company, Taiwan. Polyvinylpyrrolidone (PVP) ((C₆H₉NO)_n) (Molecular mass: Average M.W. 1,300,000; Purity: K85-95) was obtained from ACROS chemical company Taiwan.

The crystalline phases were identified with a theta-2theta X-ray diffraction meter (XRD, D₂ Phaser, Bruker, Billerica, Massachusetts, USA) using Cu K α radiation ($\lambda = 1.5406 \text{ \AA}$). After the diffraction, the data were analyzed in MDI JADE5.0 software and compared with the JCPDS Card database. A field emission scanning electron microscope (JEOL, JSM-7610F, Tokyo, Japan, and Hitachi Regulus 8100, Tokyo, Japan, respectively) was used to observe the surface, film thickness, and morphology. The working voltage was 15 kV, the working current was 10 μA , and the chamber pressure was about 1.0×10^{-6} to 3.0×10^{-6} torr. To increase the conductivity of the specimen and improve the quality of the identified image, a gold coating was deposited on the specimen with a gold coater (JFC-1600, JEOL, Tokyo, Japan). The diameter of the nanofibers was measured by ImageJ software (version: 1.54h) from SEM images. The surface area of the material was calculated by the Brunauer–Emmett–Teller (BET, Tristar II 3030, Micromeritics, Norcross, GA, USA) method using high-purity nitrogen as the adsorbate in $P/P_0 = 0.05\text{--}0.3$ under different relative pressures. A transmission electron microscope (TEM) was used at an operating voltage of 200 kV and vacuum

pressure of 10^{-8} Pa (Japan Electron Optic Co., Ltd., JEOL 2100F, Tokyo, Japan). Raman spectra were collected with a micro-Raman mapping system (ACRON, UniNanoTech Co., Ltd., Yongin-si, Korea). Thermogravimetric analysis / differential scanning calorimetry analysis was conducted (TGA/DSC) by (STA 449 F5, NETZSCH, Selb, Germany) to analyze the thermal decomposition behavior of the electrospun fibers. In the TGA experiment, the temperature was increased from room temperature to 800 °C at a heating rate of 5 °C/min with N₂/O₂. SM3030-24PIR, you-shang Technical Corp electrospinning setup with a high-speed rotating drum collector (Falco, Taipei, Taiwan) attached with a 10 mL stainless-steel needle syringe (KDS 100, KD Scientific, Holliston, USA). Electrochemical impedance spectroscopy (EIS) was carried out with the ZAHNER impedance analyzer (Kroanch, Germany) at frequencies 0.1 Hz to 1 MHz. Electrochemical studies were conducted on a CHI 1211B workstation in the N₂ atmosphere. The electrochemical work system had GCE as the main working electrode (area = 0.071 cm²), a Ag/AgCl electrode as the reference electrode, and Pt wire as the auxiliary electrode (Figure S3).

2.1. Instruments of Electrospinning

In a typical electrospinning setup, a high-voltage source was connected to a 1 mm diameter metallic needle, which was attached to a syringe pump (KDS 100, KD Scientific). In the electrospinning process, the precursor was placed in a 10 mL syringe with a stainless-steel needle. The Schematic of the electrospinning setup is shown in Figure 1. The PAN polymer solution (10 wt%) precursor fluids were prepared with the following procedure (Figure S1). First, to 0.85 g of PAN (Polyacrylonitrile, M.W. = 1,500,000), solute was added, with 7.22 mL of DMF (Dimethylformamide, from TEDIA) as the solvent, and the mixture was stirred at room temperature for 12 h to completely dissolve the polymer and obtain a viscous polymer solution (10 wt%) precursor fluid. Then, 0.3085 g of (1 mmol) Zn(NO₃)₂·6(H₂O) and 0.3287 g (4 mmol) of 2-methylimidazole were added to 25 mL methanol at room temperature and ultrasonically stirred for 10 min. Then, the precursor liquid was exposed to high-voltage electricity from a power supplier (SM3030-24PIR, you-shang Technical Corp.), with electrostatic parameters as follows: working distance, 15 cm; working voltage, 20 kV; flow rate, 0.5 mL/h; ambient temperature, 33 °C ± 2 °C; and humidity, less than 20%. The rotation speeds of the rotating collector (high-speed rotating drum collector, Falco, Taipei, Taiwan) were 500, 1000, 1500, and 2000 rpm, respectively (Figure S3). The fibers were then pre-oxidized in air at 280 °C, with a heating rate of 1 °C/min. After pre-oxidation, the prepared fibers were annealed in a N₂ atmosphere at 700 °C (Figure 2).

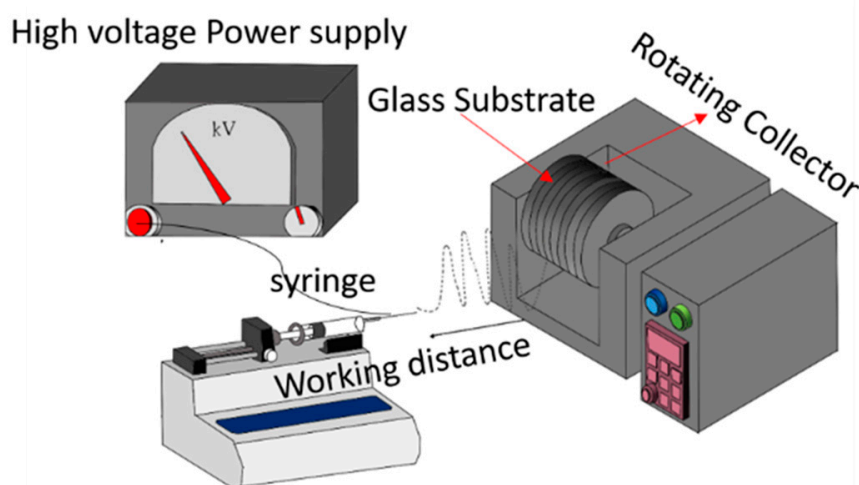


Figure 1. Schematic diagram of electrospinning of CNFs.

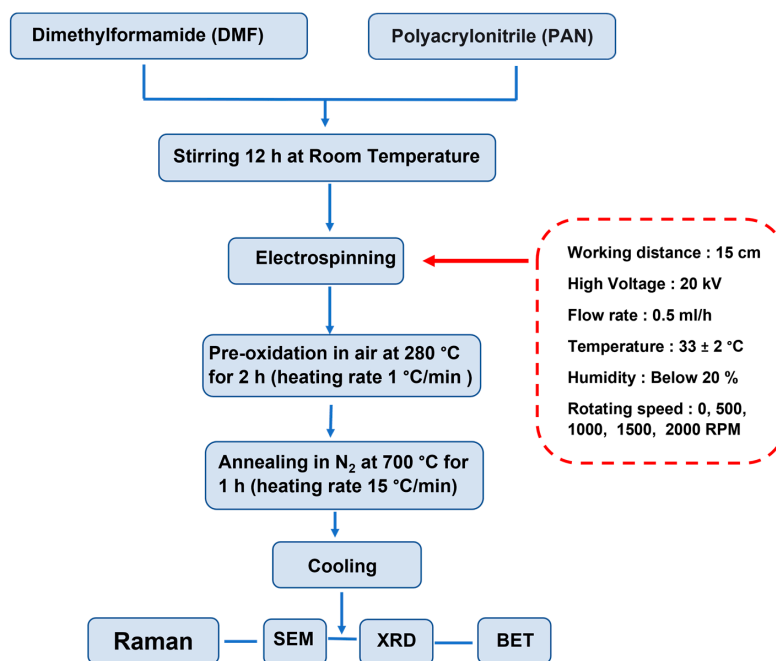


Figure 2. Flow chart for straight and unidirectional CNF fabrication.

2.2. Preparation of ZIF-8

ZIF-8 was prepared by a synthesis method using a methanol solution at a normal temperature and pressure. First, 0.3085 g (1 mmol) of zinc nitrate hexahydrate was dissolved in methanol and ultrasonically stirred for 10 min to form a zinc nitrate solution, labeled solution A (Figure S2). Furthermore, 0.3287 g (4 mmol) of 2-methylimidazole was mixed in methanol at room temperature and ultrasonically stirred for 10 min to form solution B. After that, the zinc nitrate solution (solution A) and methylimidazole solution (solution B) were mixed under rapid stirring at room temperature for 2 h before being filtered to obtain a white powder. This powder was washed with methanol 5 to 10 times and finally dried at 60 °C for 24 h (Figure 3). After the ZIF-8 powder cooled to room temperature, it was stored for further use.

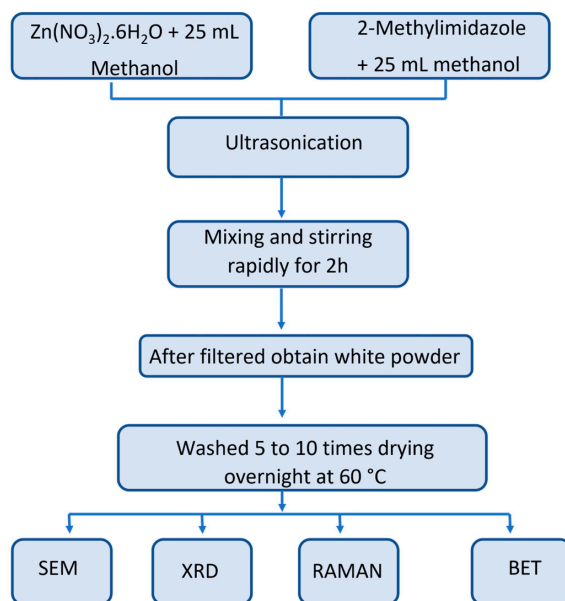


Figure 3. Flow chart for preparation of ZIF-8.

2.3. Preparation of ZIF-8/CNF Composite

ZIF-8/CNF composites were prepared from 0.3085 g of zinc nitrate hexahydrate, 2-methylimidazole, and methanol. First, synthesized CNFs (10 mg, 15 mg, or 20 mg) and approximately 1 mmol of zinc nitrate hexahydrate were added to 25 mL methanol. Then, the mixture was ultrasonically stirred at room temperature for 10 min to form the zinc nitrate hexahydrate precursor solution. After that, 4 mmol of 2-methylimidazole was added to methanol at room temperature and ultrasonically stirred for 10 min before quickly being mixed into the solutions of zinc nitrate hexahydrate. The mixtures were stirred at room temperature for 2 h and filtered to obtain white powder, which was washed with methanol 5 to 10 times before being dried at 60 °C for 24 h. The resulting ZIF-8/CNF composite material was stored and used for further studies. The schematic representation of the synthesis of the ZIF-8/CNFs composite is shown in Figure 4.

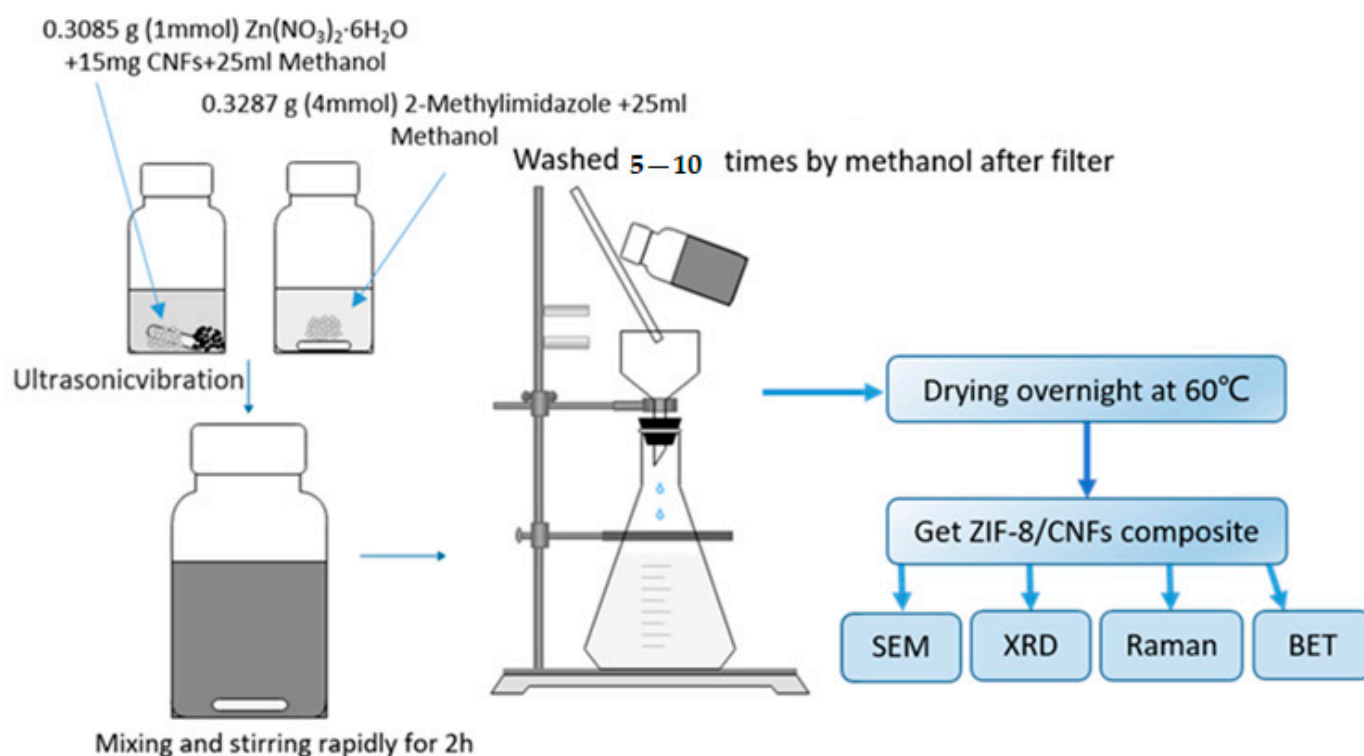
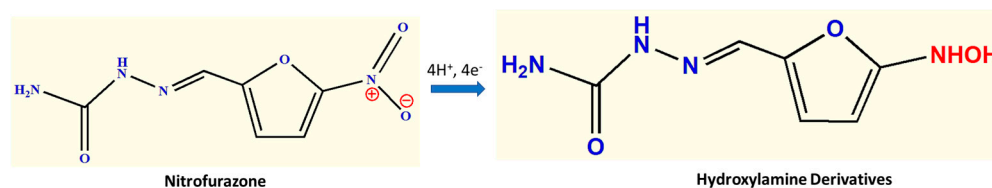


Figure 4. Flow chart for preparation of ZIF-8/CNF composite.

2.4. Preparation of GCE/ZIF-8/CNF Electrode

The GCE/ZIF-8/CNF electrode was prepared with the following process. The bare GCE surface was first polished with a 0.5 μm size alumina slurry ($\alpha\text{-Al}_2\text{O}_3$) before being dipped in DI water and dried at room temperature for further modification. The prepared ZIF-8/CNFs catalyst (5 mg) was dispersed in 10 mL of DMF and ultrasonicated for 30 min. After that, 5 μL , 8 μL , and 10 μL of the ZIF-8/CNF material dispersion were drop-cast onto the cleaned GCE surface and dried at laboratory temperature. Then, the prepared GCE/ZIF-8/CNF electrodes were applied to the electrochemical sensor studies. The details of the preparation of the GCE/ZIF-8/CNF electrode are provided in Scheme 1. For comparison studies, GCE/ZIF-8 and GCE/CNF electrodes were prepared with the same procedure. Then, 8 μL of electrode-material-coated GCE/ZIF-8, GCE/CNF, and GCE/ZIF-8/CNF modified electrodes were used for the FLT sensor.



Scheme 1. Electrochemical detection of nitrofurazone over GCE/ZIF-8/CNF composite electrode.

3. Results and Discussion

3.1. TGA Analysis of Carbon Nanofibers

Figure S5 shows the Differential Scanning Calorimetry—Thermogravimetric Analysis (DSC-TGA) results for PAN nanofibers in air. Figure 5 presents the DSC-TGA graph of PAN nanofibers, which shows almost no weight loss before 130 °C. When the temperature was between 130 °C and 230 °C, the DMF solvent began to volatilize at the same time the PAN underwent physical shrinkage and chemical cyclization shrinkage. Therefore, a weight loss of nearly 5% was indicated on the TGA curve between 130 °C and 230 °C. When the temperature rose to 230–300 °C, the fibers exhibited 10% weight loss as they underwent cyclization, dehydrogenation, and oxidation reactions. The H and N elements were removed and a stable PAN molecular chain structure was formed. At temperatures between 300 °C and 470 °C, the C, H, and N elements reacted with O₂ to generate gas, and the PAN fiber was completely decomposed. Thus, we pre-oxidized the spun fibers at 280 °C before carbonization. Generally, the pre-oxidation temperature should be about 260 °C; otherwise, the PAN fiber will be melted or even ablated.

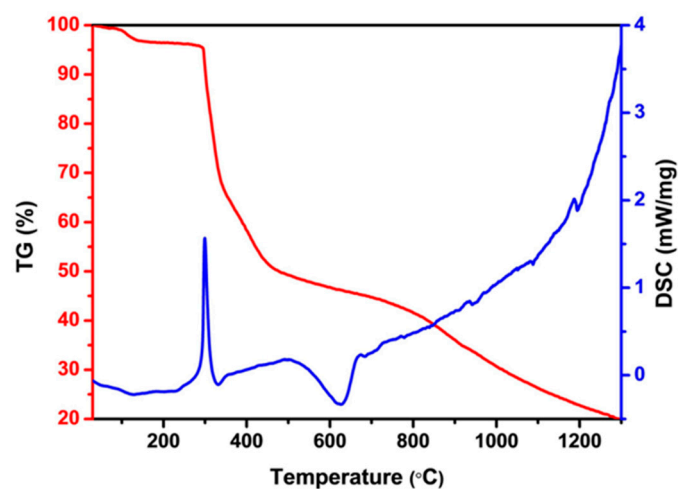


Figure 5. The DSC-TGA results for PAN nanofibers in 5 °C/min with N₂/O₂ and Ar used for the reaction (Blue line for DSC and red line for TGA curve).

3.2. SEM and TEM Analysis

Figure 6 presents (A) SEM images of as-spun CNFs (2000 rpm), (B–D) SEM images of CNFs after annealing, and (E–F) SEM images of a ZIF-8 crystal. SEM images of 500 rpm, 1000 rpm, and 1500 rpm CNFs after annealing are shown in Figure S5, Figure S6 and Figure S7, respectively. The SEM image of the as-spun fibers shows that the average fiber diameter was about 100–700 nm. The overall diameter of the as-spun fibers was uniform, and there was no agglomeration or adhesion. After pre-oxidation and annealing at a rate of 1 °C/min to 280 °C in air for pre-oxidation and subsequent heating at a rate of 1 °C/min to 280 °C in a N₂ atmosphere for carbonization, the residual DMF and moisture disappeared due to pre-oxidation and the PAN was carbonized after high-temperature annealing. The average fiber diameter was about 100–420 nm. In addition, the CNFs did not break and the overall diameter remained the same after annealing. The rotation speed gradually increased, and the CNFs became straight and unidirectional in the experiment.

Additionally, with increases in the rotation speed, the diameter of the CNFs did not change significantly. Figure S10 shows the SEM images of (a) the ZIF-8/(10 mg)/CNF composite, (b) the ZIF-8/(15 mg)/CNF composite, and (c) the ZIF-8/(20 mg)/CNF composite prepared at a normal temperature and pressure. Figure 6E,F shows that ZIF-18 had a hexagonal crystalline structure with an overall diameter of about 50–115 nm.

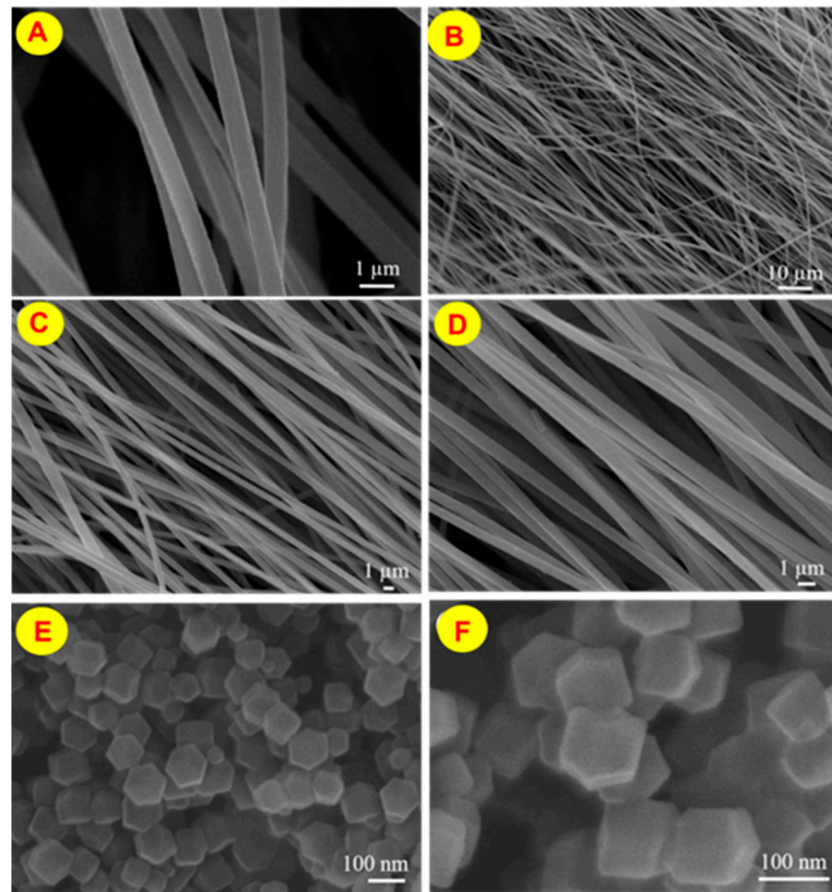


Figure 6. SEM images of (A) electrospun-prepared CNFs (2000 rpm), (B–D) SEM images of CNFs (2000 rpm) after annealing, and (E,F) SEM images of ZIF-8 crystal.

The ZIF-8/CNF composite was successfully generated by the synthesis method of methanol solution at normal temperature and pressure after improvement. Figure 7A–D shows SEM images of the ZIF-8/CNFs composite, revealing that the structure of the crystal attached to the surface of the composite was similar to the simulated ZIF-8 structure and indicating that, before and after composition, the CNFs remained unbroken and the overall diameter stayed the same. The results of the SEM images indicated the following: the CNFs were about 15 mg, mutual accumulation of ZIF-8 occurred, the weight of the CNFs was about 20 mg, and some CNFs had no ZIF-8 crystals attached to the surfaces. ZIF-8 was less attached to the surface of CNFs but accumulation between CNFs and ZIF-8 still occurred. The ZIF-8 crystals were relatively uniformly attached on the surfaces of CNFs, and the mutual accumulation between ZIF-8 and CNFs was relatively rare and would be used in the next analysis. The TEM image of the ZIF-8/CNFs composite confirmed that some particles were arranged on the CNFs surfaces and attached to them. TEM images of ZIF-8/CNFs composite fabricated by the synthesis method of methanol solution at normal temperature and pressure after improvement showed that the ZIF-8 crystals were relatively uniformly attached on the surface of the CNFs and mutual accumulation occurred between the CNFs and ZIF-8.

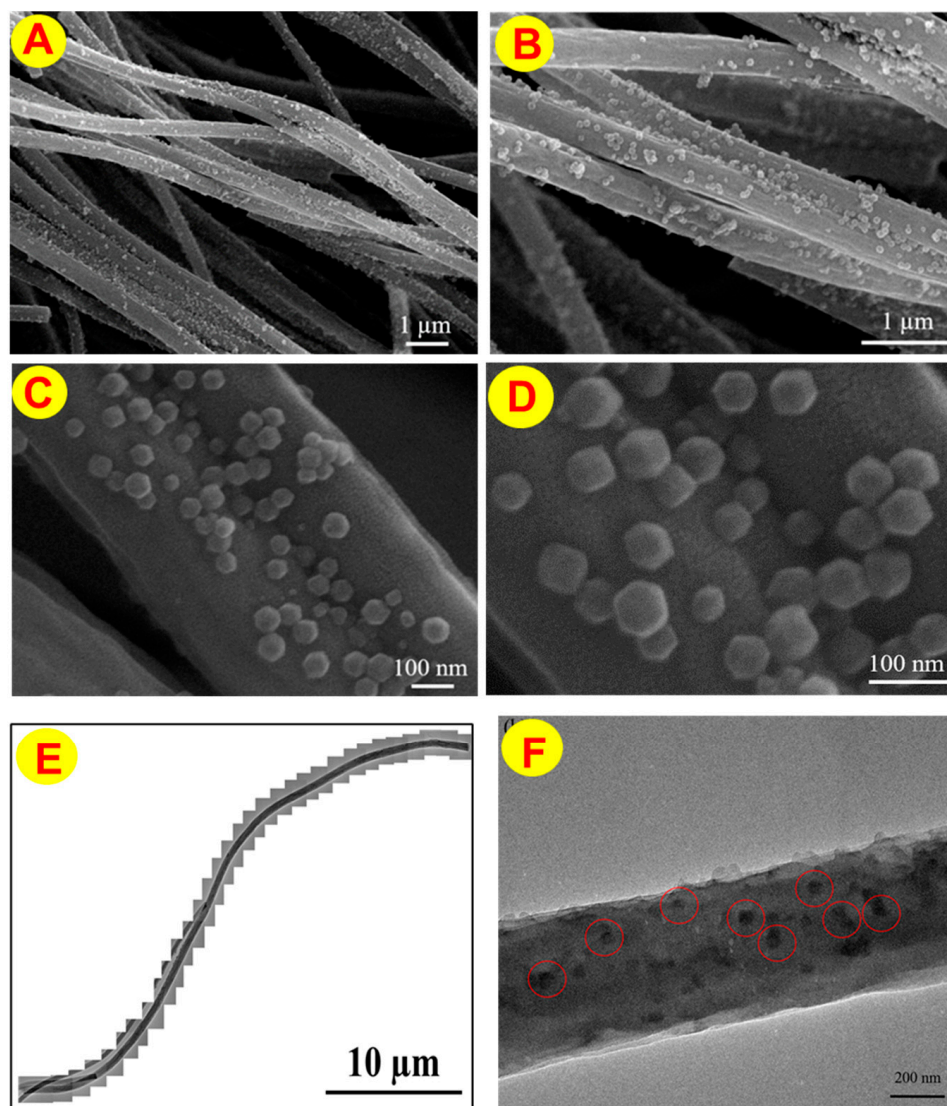


Figure 7. (A–D) SEM images of the ZIF-8/CNF composite prepared at normal temperature and pressure. (E,F) TEM images of the ZIF-8/CNF composite.

3.3. XRD Studies

Figure 8 presents the XRD patterns of ZIF-8, the CNFs, and the ZIF-8/CNF composite. The XRD pattern of CNFs after annealing showed no obvious diffraction peaks. Figure S8 shows the XRD patterns of CNFs prepared by electrospinning. Because the CNFs were an amorphous material and had undergone high-temperature annealing carbonization, they presented no obvious crystallinity. The diffraction peak of the rhombohedral phase generated by the synthesis method of methanol solution at normal temperature and pressure was consistent with the diffraction peak of the simulated ZIF-8 (PDF#62-1030). The main diffraction peaks at 7.3° , 10.4° , 12.7° , 14.3° , 16.4° , and 17.9° corresponded to the (110), (200), (211), (220), (310), and (222) planes of ZIF-8. As shown in the XRD spectra, the diffraction peaks of the ZIF-8/CNF composite were similar to the theoretical diffraction peaks of simulated ZIF-8. In addition, the CNFs, being an amorphous material, exhibited low crystallinity and their diffraction peaks were covered by the diffraction peaks of ZIF-8. These results indicated that the ZIF-8 crystals were successfully attached to the surfaces of the CNFs.

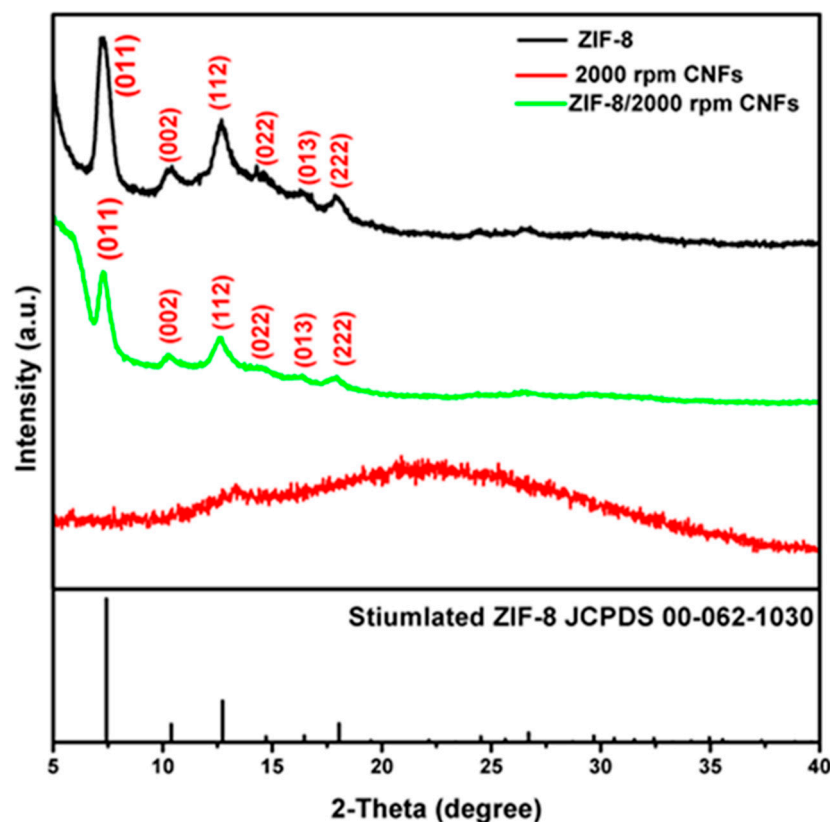


Figure 8. The XRD patterns of ZIF-8, CNFs, and ZIF-8/CNFs composite fabricated by synthesis method of methanol solution at normal temperature and pressure.

3.4. Raman Spectra

The Raman spectra of the simulated ZIF-8, CNFs, and ZIF-8/CNF composite are shown in Figure 9. Further to study the characteristics and microstructure of the amorphous CNFs, the graphitization degree of the CNFs was evaluated by Raman spectroscopy. Figure S9 shows the Raman spectrum of annealed CNFs prepared by electrospinning in 2000 rpm conditions. The Raman spectrum of ZIF-8 shows that strong bands are observed at 686 cm^{-1} , 1146 cm^{-1} , and 1458 cm^{-1} in the range of $400\text{--}2000\text{ cm}^{-1}$. These bands are corresponding to the bending vibration of the imidazole ring, $\text{C}_5\text{-N}$ stretching vibration, methyl bending vibration, antisymmetric vibration of C-H , and C-H stretching vibration, respectively. Further, the Raman spectrum of the CNFs revealed two strong D and G peaks at 1340 cm^{-1} and 1576 cm^{-1} , respectively. In these spectra, the D-band for lattice defects and G band for the sp^2 hybridized carbon atoms stretching vibration, respectively. The area between peak D and peak G (I_D/I_G) is usually used to describe the level of graphitization of carbon. A carbon material with a large value of I_D/I_G possesses many defect sites, which are beneficial to surface catalytic reactions. Moreover, the Raman spectrum of the ZIF-8/CNF composite depicted the curve of ZIF-8 and CNFs. The band at 686 cm^{-1} was related to the out-of-plane bending vibration of the imidazolate ring. The spectral region from $1100\text{ to }1200\text{ cm}^{-1}$ indicated the C-N stretching vibration from the imidazolate ring. The band at 1461 cm^{-1} was due to the C-H vibration of the methyl group. In addition, there should be a signal of C=C stretching vibration from the imidazolate ring at about 1500 cm^{-1} . The ZIF-8/CNF composite mainly had two strong peaks similar to those of CNFs. They were the D peak at 1340 cm^{-1} and the G peak at 1576 cm^{-1} . The Raman spectral studies indicated the successful formation of the ZIF-8/CNF composite.

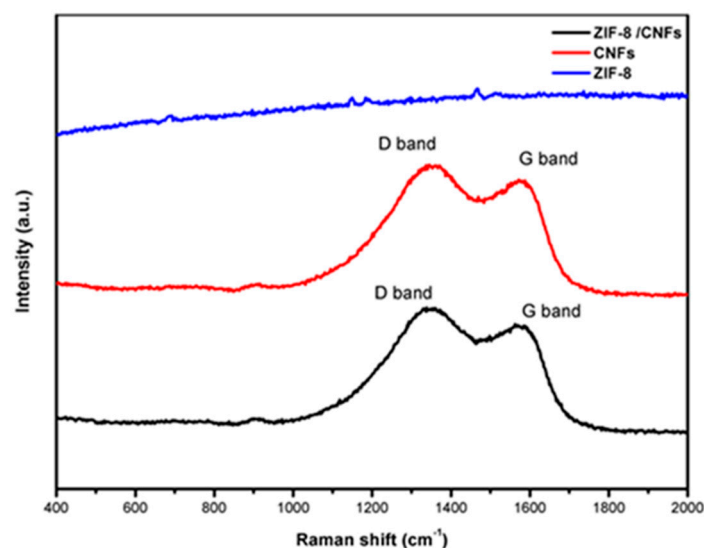


Figure 9. The Raman spectra of simulated ZIF-8, CNFs, and ZIF-8/CNF composite.

3.5. BET Analysis

The surface areas of the ZIF-8/CNF (2000 rpm) composite determined by BET are listed in Table 1. High-purity N_2 gas was flowed over the ZIF-8/CNF catalyst at $150\text{ }^\circ\text{C}$ for 12 h. The N_2 gas adsorption volume was measured using $P/P_0 = 0\text{--}0.3$ under various relative pressures. The results showed that due to the ZIF-8 being successfully attached to the CNFs and the consequently extremely high specific surface area, the specific surface area of the ZIF-8/CNF catalyst varied from $42.28\text{ m}^2/\text{g}$ to $999.82\text{ m}^2/\text{g}$. Based on the BET studies, pure CNFs, and ZIF-8 exhibited 42.28 and 1310.34 , respectively. On the other hand, if ZIF-8/(10 mg) were attached to the CNFs, the higher specific surface area of ZIF-8/(15 mg)/CNFs would be reduced because CNFs would accumulate and cover the ZIF-8 pores on the surfaces by the CNFs. After that, the specific surface area of the ZIF-8/(15 mg)/CNF composite reached a higher $999.82\text{ m}^2/\text{g}$ because of ZIF-8 and the CNFs, having uniformly attached to form ZIF-8/CNF composite. Moreover, the higher specific surface area of ZIF-8/(20 mg)/CNFs would be reduced at $216.74\text{ m}^2/\text{g}$ due to the higher ratio level of ZIF-8 and its irregular combination with CNFs. Hence, the higher specific surface area of ZIF-8/(15 mg)/CNFs exhibited higher electrochemical performances. Therefore, we applied ZIF-8/(15 mg)/CNF catalysts for further electrochemical sensors of NFZ [53–55].

Table 1. The specific surface area of ZIF-8/CNF composite.

Composition	Specific Surface Area (m^2/g)
2000 rpm CNFs	42.28
Simulated ZIF-8	1310.34
ZIF-8/(10 mg) 2000 rpm CNFs	333.53
ZIF-8/(15 mg) 2000 rpm CNFs	999.82
ZIF-8/(20 mg) 2000 rpm CNFs	216.74

4. Electrochemical Analysis of ZIF-8/CNFs Composite toward NFZ

4.1. Electrochemical Performance of NFZ at Modified Electrodes

The CV curves of various electrodes in NFZ were determined by the cyclic voltammetry technique. Figure 10A shows the cyclic voltammetric behaviors of bare GCE, GCE/CNFs, GCE/ZIF-8, and GCE/ZIF-8/CNFs composite in $40\text{ }\mu\text{M}$ of NFZ with N_2 purging of 0.5 M PBS at a scan rate of 50 mVs^{-1} . At the bare GCE, the redox couple was not observed, as the bare electrode was not responsive to NFZ. The GCE/CNFs and

GCE/ZIF-8 electrodes had reduction peaks of NFZ of 110 μA and 152 μA , respectively. The GCE/ZIF-8/CNFs composite electrode had an excellent electrochemical response to NFZ (compared with other electrodes) with a reduction peak at 216 μA . Here, the reason for the good response was the high surface area of the material and good conduction for easy electron transfer. The CNFs and ZIF-8 were used due to their high surface area and increased electron transfer process. Thus, the electrochemical performances of the GCE/ZIF-8/CNF composite were better than those of the other electrode materials. For comparison, Figure 10B shows the responses of the bare GCE and the GCE/ZIF-8/CNFs composite electrodes toward NFZ detection (Scheme 1).

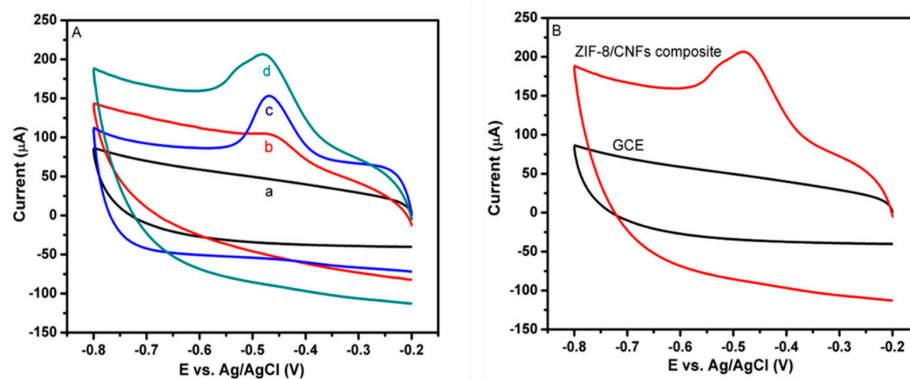


Figure 10. (A) CV studies of (a) bare GCE, (b) GCE/CNFs, (c) GCE/ZIF-8, (d) GCE/ZIF-8/CNF composite electrode in the presence of 40 μM of NFZ in 0.5 M PBS (pH = 7.0) at a scan rate of 50 mVs^{-1} , and (B) CV responses of GCE and GCE/ZIF-8/CNFs composite in the presence of NFZ in PBS (pH = 7.0) at a scan rate of 50 mVs^{-1} .

4.2. Effects of Different Scan Rates

Figure 11A presents the various scan rates of electrochemical studies in the modified GCE/ZIF-8/CNF composite electrode in pH 7.0 (0.5 M PBS) consisting of 40 μM NFZ at scan rates of 10–200 mVs^{-1} . From the results, it is clear that the peak current uniformly increased as the scan rate shifted the potential toward the negative side. Figure 11B compares the linear plot for the redox peak of current with the square root of the scan rate. The results indicated a linear regression equation $I_p = 22.826x - 38.528$ and an R^2 value of 0.9919. These results confirmed that the detection process of GCE/ZIF-8/CNFs composite electrodes was diffusion-controlled. These results indicated good electronic and catalytic activity.

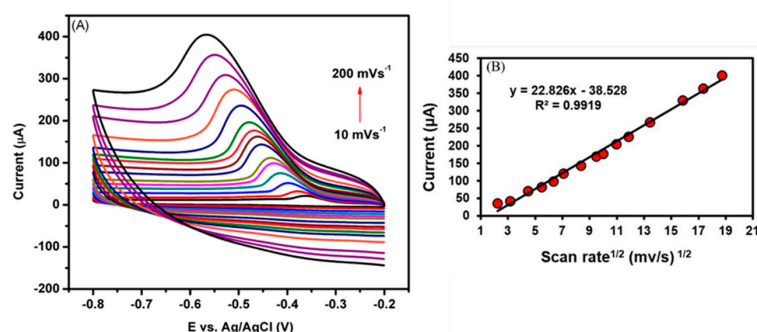


Figure 11. (A) CV curves of GCE/ZIF-8/CNFs electrode in the presence of 40 μM NFZ in 0.5 M PBS (pH 7.0) were observed at scan rates of 10–200 mVs^{-1} . (Different colors are mentioned for different scan rates of 10–200 mVs^{-1}). (B) Correlations between the peak currents and the square root of the scan rate.

Figure 12A presents the electrochemical performances for the detection of NFZ with different concentrations. Increasing the concentration of the NFZ further increased the

current of the GCE/ZIF-8/CNF electrode. Without the addition of NFZ, no redox peak was evident. Each addition of NFZ raised the peak current of the electrode. These results demonstrated the excellent electrochemical performance of the GCE/ZIF-8/CNF electrode. Figure 12B reveals the corresponding linear relation between the peak current and NFZ concentration, and the calculated R^2 value was 0.9909. These results indicated that the GCE/ZIF-8/CNFs electrode exhibited excellent electrochemical performance for the detection of NFZ.

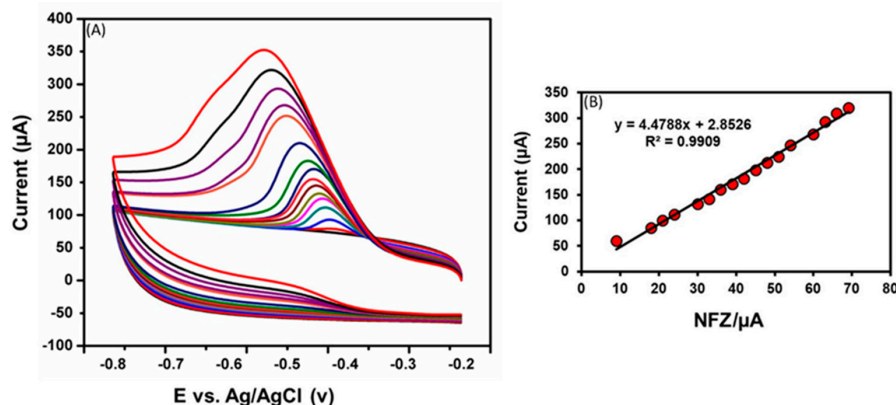


Figure 12. (A) Effects of different concentrations (10–70 μM) at the GCE/ZIF-8/CNF electrode for the detection of NFZ at a scan rate of 50 mVs^{-1} in 0.5M PBS (pH = 7.0) (Different colors mentioned for different concentrations of NFZ). (B) Calibration plot between the peak current and the NFZ concentration.

4.3. Electronic Analysis under Varied PH

The electrochemical behavior of the GCE/ZIF-8/CNF electrode was further evaluated at different pH conditions (pH 3.0–11.0) in CV for 40 μM NFZ, and the results are shown in Figure 13A. It could be seen that the redox peak current increased as the pH rose from 3 to 11. Furthermore, the redox potential also shifted in the negative direction between pH 3 and pH 7, after which the peak current decreased until pH 11. This indicated that the electrochemical behavior depended on the pH of the solution. The ZIF-8/CNFs composite was much more active at pH 7. Hence, pH 7 was used for further electrochemical studies of NFZ detection with the GCE/ZIF-8/CNF electrode. Figure 13B shows that the maximum peak current response for the detection of NFZ was obtained at pH 7. Also, the linear relation obtained for the peak potential versus pH (Figure 13C) suggested that the non-dissociated NFZ was adsorbed more over the GCE/ZIF-8/CNF composite electrode.

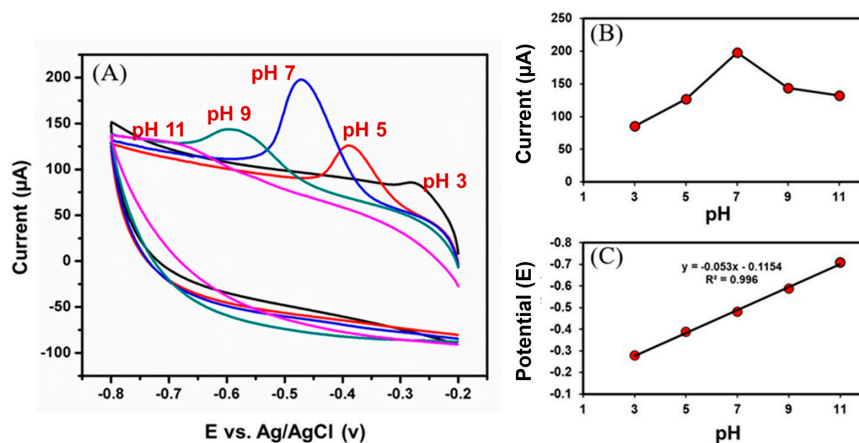


Figure 13. (A) Cyclic voltammogram of GCE/ZIF-8/CNF electrode under deoxygenated conditions at pH 3.0 to pH 11.0. (B) The inset shows the pH values versus peak current. (C) The inset shows the pH values versus redox potential.

4.4. DPV Studies and Stability Studies

DPV is a more sensitive method than the CV technique. DPV was used to measure the minimum and maximum detectable concentrations of NFZ. Figure 14A presents the DPV curve of the GCE/ZIF-8/CNF composite electrode under different concentrations (0.1–150 μM) of NFZ in 0.5M of PBS. The figure shows the sharp peak of the cathodic reduction current of NFZ. The results confirmed that the GCE/ZIF-8/CNF composite electrode had excellent sensitivity to NFZ for $15.55 \mu\text{A} \mu\text{M}^{-1} \text{cm}^{-2}$ and a limit of detection (LOD) of $0.027 \mu\text{M}$. Figure 14B shows that the obtained linear regression equation was $I(\mu\text{A}) = 1.8096x - 6.4888$ [NFZ]/ μM , with a correlation coefficient of 0.99. The sensitivity was calculated as $15.55 \mu\text{A} \mu\text{M}^{-1} \text{cm}^{-2}$ with an LOD of $0.027 \mu\text{M}$. The GCE/ZIF-8/CNF electrode exhibited better performance in sensing NFZ than did the previously reported modified electrodes listed in Table 2. The detection limit ($0.027 \mu\text{M}$) of the NFZ at the GCE/ZIF-8/CNFs electrode is lower than that of the other modified electrodes such as $\text{Ag}^+@\text{UiO}-66 \text{NH}_2/\text{CsPbBr}_3/\text{GCE-ECL}$ (LOD = $90 \mu\text{M}$), Ag-NPs@CPE (LOD = $0.012 \mu\text{M}$), $\text{MIP-c-MWCNTs-ZIF/GCE}$ (LOD = $6.7 \mu\text{M}$), Fe-MOF/rGO/SPCE (LOD = $90 \mu\text{M}$), $\text{Ag}_2\text{S QDs/g-C}_3\text{N}_4$ (LOD = $0.054 \mu\text{M}$), Poly-ACBK/GCE (LOD = $0.25 \mu\text{M}$), Au-Ag (LOD = $0.2 \mu\text{M}$), Ag-SDS (LOD = $0.37 \mu\text{M}$), $\text{ZnCr}_2\text{O}_4/\text{SPCE}$ (LOD = $0.001 \mu\text{M}$), and DUT-67/T-PPY/GCE (LOD = $0.25 \mu\text{M}$), due to the higher electrocatalytic activity as well as large surface area.

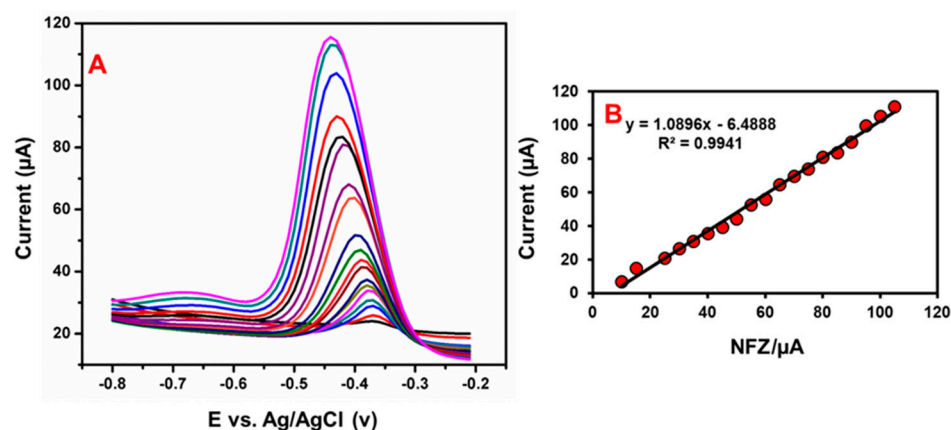


Figure 14. (A) The DPV performance of the GCE/ZIF-8/CNF electrode in different concentrations of NFZ. (B) The plot of the peak current versus concentration of NFZ. Different colors are mentioned for different concentrations (0.1–150 μM) of NFZ.

Table 2. Comparison of GCE/ZIF-8/CNF electrode with other NFZ electrochemical sensors.

S. No	Electrode	LOD (μM)	Linear Range (μM)	Ref.
1	GCE/ZIF-8/CNFs	0.027	0.1–150	This Work
2	Ag-NPs@CPE	0.012	0.2–100	[56]
3	$\text{Ag}^+@\text{UiO}-66\text{-NH}_2/\text{CsPbBr}_3/\text{GCE-ECL}$	90	5×10^{-4} –100	[57]
4	MIP-c-MWCNTs-ZIF/GCE	6.7	-	[3]
5	Fe-MOF/rGO/SPCE	0.77	0.6–499	[58]
6	$\text{Ag}_2\text{S QDs/g-C}_3\text{N}_4$	0.054	0–30	[59]
7	Poly-ACBK/GCE	0.25	0.75–192	[4]
8	Au-Ag	0.2	1.99–643	[60]
9	Ag-SDS	0.37	0.66–930	[61]
11	$\text{ZnCr}_2\text{O}_4/\text{SPCE}$	0.001	0.01–152	[62]
12	DUT-67/T-PPY/GCE	0.25	9.08–1004	[5]

Cyclic stability is a major factor in electrochemical sensor studies. The obtained results indicated good operational stability. As shown in Figure 15, which presents the results of

stability electronic analysis, during the first three cycles, the position and intensity of the redox peak corresponding to the GCE/ZIF-8/CNFs electrode were almost unchanged, and after the first cycle, the CV curves overlapped well. After 50 cycles of charge and discharge, the GCE/ZIF-8/CNFs electrode still had good cyclic stability.

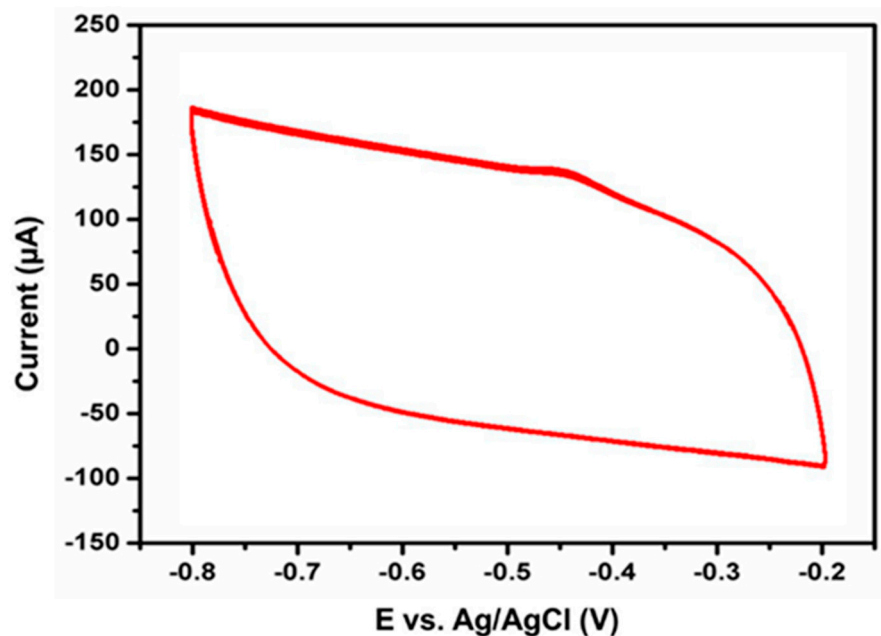


Figure 15. Cyclic stability studies of the GCE/ZIF-8/CNFs electrode during detection of NFZ at a scan rate of 50 mVs^{-1} in PBS (pH = 7.0) for 50 cycles.

4.5. Real Sample Analysis, Repeatability and Reproducibility

Figure 16 shows the GCE/ZIF-8/CNF electrode performance, after being evaluated by the DPV technique to detect NFZ in milk, river water, and tap water samples. Here, NFZ real samples were detected using the standard addition approach. Under ideal conditions, real sample analysis was carried out at laboratory temperature. The obtained milk and water samples were utilized for the analysis after being diluted to pH 7.0. Additionally, NFZ real sample measurements were carried out using electrochemical detection. Increasing the NFZ concentration increased the reduction peak current. The obtained results are listed in Table 3. The recovery results on milk (99.4%), tap water (98.4%), and river water (99.3%) revealed that the real sample recovery values for the sensing of NFZ were acceptable. This result demonstrated that the GCE/ZIF-8/CNF electrode is a promising option for electrochemically detecting NFZ in a variety of samples, even though these techniques have benefitted from such a high sensitivity, low cost, quick detection, short response time, outstanding selectivity, and ease of use.

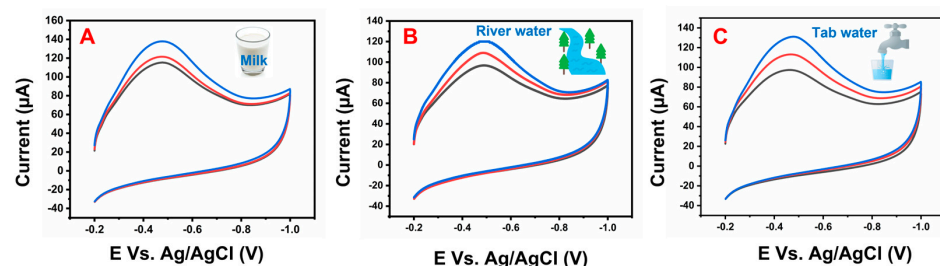


Figure 16. Electrochemical sensing of NFZ with the GCE/ZIF-8/CNF electrode in (A) milk, (B) river water, and (C) tap water. Different colors are mentioned for different addition (40 μM , 80 μM , 120 μM) of real samples.

Table 3. Real sample analysis of NFZ in milk and water samples.

Sample	Added (μM)	Found (μM)	Recovery (%)
Milk	40	39.8	99.5
	80	79.3	99.2
	120	119.5	99.5
River water	40	39.0	97.5
	80	78.9	98.6
	120	119.2	99.3
Tap Water	40	39.5	98.7
	80	79.6	99.5
	120	119.8	99.8

Figure S11 shows the repeatability and reproducibility performance of the GCE/ZIF-8/CNFs electrode, after being evaluated by CV studies in the presence of 20 μM NFZ in PBS (pH 7). The GCE/ZIF-8/CNFs electrode had acceptable repeatability for four consecutive measurements by a single modified electrode. Furthermore, the GCE/ZIF-8/CNFs electrode showed considerable reproducibility in four experiments performed with four separate modified electrodes. According to the studies, the GCE/ZIF-8/CNFs electrode exhibited good repeatability and reproducibility performances.

5. Conclusions

In this study, we successfully produced as-spun carbon fibers by electrospinning and controlling the rotation speed of the rotating collector, and then we used pre-oxidation treatment at 280 $^{\circ}\text{C}$ and annealing at 700 $^{\circ}\text{C}$ under a N_2 atmosphere to obtain CNFs. According to the XRD, FESEM, and Raman spectroscopy studies, the ZIF-8/CNF composite was successfully formed, and the ZIF-8 crystals were uniformly attached to CNFs. The specific surface areas of the ZIF-8, the CNFs, and the ZIF-8/CNF composite materials were calculated. The specific surface area of the ZIF-8/CNFs composite reached 999.82 m^2/g . The ZIF-8/CNF composite had a better performance in catalytic activity and electrochemical characteristics. Electrochemical analysis showed that the synthesized ZIF-8/CNF composite nanomaterial had a wide linear response range; good stability, sensitivity, and selectivity; and great potential for electrochemical applications. The GCE/ZIF-8/CNFs electrode exhibited an excellent electrochemical response for the detection of nitrofurazone with a linear range of 0.1–150 μM , limit of detection of 0.027 μM , and sensitivity of 15.55 $\mu\text{A } \mu\text{M}^{-1} \text{cm}^{-2}$.

Supplementary Materials: The following supporting information can be downloaded at: <https://www.mdpi.com/article/10.3390/micro4010002/s1>, Figure S1: Schematic diagram of the PAN/DMF precursor preparation.; Figure S2: Schematic diagram of the electrospinning setup; Figure S3: Photograph of electrochemical studies; Figure S4: The DSC-TGA results for PAN nanofibers in the air; Figure S5: SEM images of 500 rpm CNFs after annealing; Figure S6: SEM images of 1000 rpm CNFs after annealing; Figure S7: SEM images of 1500 rpm CNFs after annealing; Figure S8: The XRD patterns of CNFs prepared by electrospinning; Figure S9: The Raman spectrum of before annealed CNFs prepared by electrospinning at 2000 rpm.; Figure S10: SEM images of (a) ZIF-8/(10 mg)/CNFs composite, (b) ZIF-8/(15 mg)/CNFs composite, (c) ZIF-8/(20 mg)/CNFs composite prepared at normal temperature and pressure.; Figure S11: (A) The CV curve of GCE/ZIF-8/CNFs electrode in the presence of the NFZ repeatability test. (B) Four different GCE/ZIF-8/CNFs electrodes for reproducibility test.

Author Contributions: Conceptualization, H.W., S.S., A.K.K. and C.-L.Y.; methodology, H.W., S.S. and A.K.K.; software, H.W., A.K.K. and C.-L.Y.; validation, S.S., A.K.K., C.-L.Y. and T.-W.C.; formal analysis, H.W., S.S., A.K.K. and C.-L.Y.; investigation, H.W., S.S. and A.K.K.; resources, H.W., S.S., A.K.K. and C.-L.Y.; data curation, H.W., S.S., A.K.K., C.-L.Y., T.-W.C. and K.N.; writing—original draft preparation, H.W., S.S., A.K.K., C.-L.Y., T.-W.C., K.N. and S.K.; writing—review and editing, H.W., S.S., A.K.K., C.-L.Y., T.-W.C. and K.N.; visualization, S.S., A.K.K., C.-L.Y. and S.K.; supervision,

T.-W.C.; project administration, S.S., T.-W.C. and K.N.; funding acquisition, T.-W.C. All authors have read and agreed to the published version of the manuscript.

Funding: This work was supported by the National Science and Technology Council Taiwan (NSTC-112-2221-E-027-039 and NSTC 112-2221-E-027-032). The authors are grateful to the Precision Research and Analysis Centre of the National Taipei University of Technology (NTUT) for providing the measurement facilities.

Data Availability Statement: Dataset available on request from the authors.

Acknowledgments: This work was supported by the National Science and Technology Council Taiwan. The authors are grateful to the Precision Research and Analysis Centre of the National Taipei University of Technology (NTUT) for providing the measurement facilities.

Conflicts of Interest: The authors declare no conflicts of interest.

References

1. Keyan, A.K.; Sakthinathan, S.; Vasu, D.; Yu, C.L.; Vinothini, S.; Chiu, T.W. Gadolinium molybdate decorated graphitic carbon nitride composite: Highly visualized detection of nitrofurazone in water samples. *RSC Adv.* **2022**, *12*, 34066–34079. [[CrossRef](#)] [[PubMed](#)]
2. Zoubir, J.; Assabbane, A.; Bakas, I. Electroanalysis of nitrofurazone at silver particles and graphite powder composite electrode. *Carbon Lett.* **2022**, *32*, 767–780. [[CrossRef](#)]
3. Lu, H.; Liu, M.; Cui, H.; Huang, Y.; Li, L.; Ding, Y. An advanced molecularly imprinted electrochemical sensor based bifunctional monomers for highly sensitive detection of nitrofurazone. *Electrochim. Acta* **2022**, *42*, 7140858. [[CrossRef](#)]
4. Wang, Y.; Guo, Y.; Pan, K.; Lin, X.; Ni, Y. Electrochemical Reaction Mechanism of Nitrofurazone at Poly-ACBK/GCE and Its Analytic Application. *Chem. Afr.* **2020**, *3*, 727–734. [[CrossRef](#)]
5. Wang, H.; Bo, X.; Zhou, M.; Guo, L. DUT-67 and tubular polypyrrole formed a cross-linked network for electrochemical detection of nitrofurazone and ornidazole. *Anal. Chim. Acta* **2020**, *1109*, 1–8. [[CrossRef](#)]
6. Hartmann, M.; Machoke, A.G.; Schwieger, W. Catalytic test reactions for the evaluation of hierarchical zeolites. *Chem. Soc. Rev.* **2016**, *45*, 3313–3330. [[CrossRef](#)]
7. Ruehle, B.; Clemens, D.L.; Lee, B.Y.; Horwitz, M.A.; Zink, J.I. A Pathogen-Specific Cargo Delivery Platform Based on Mesoporous Silica Nanoparticles. *J. Am. Chem. Soc.* **2017**, *139*, 6663–6668. [[CrossRef](#)]
8. Sun, Y.; Ma, K.; Kao, T.; Spoth, K.A.; Sai, H.; Zhang, D.; Kourkoutis, L.F.; Elser, V. Formation pathways of mesoporous silica nanoparticles with dodecagonal tiling. *Nat. Commun.* **2017**, *8*, 252. [[CrossRef](#)]
9. Li, B.; Wen, H.M.; Cui, Y.; Zhou, W.; Qian, G.; Chen, B. Emerging Multifunctional Metal–Organic Framework Materials. *Adv. Mater.* **2016**, *28*, 8819–8860. [[CrossRef](#)]
10. Allendorf, M.D.; Stavila, V. Crystal engineering, structure-function relationships, and the future of metal-organic frameworks. *Cryst. Eng. Commun.* **2015**, *17*, 229. [[CrossRef](#)]
11. Furukawa, H.; Cordova, K.E.; Keeffe, M.O.; Yaghi, O.M. The chemistry and applications of metal-organic frameworks. *Science* **2013**, *30*, 1230444. [[CrossRef](#)] [[PubMed](#)]
12. Venna, S.R.; Carreon, M.A. Metal organic framework membranes for carbon dioxide separation. *Chem. Eng. Sci.* **2015**, *124*, 3–19. [[CrossRef](#)]
13. Liu, X.; Yang, H.; Diao, Y.; He, Q.; Lu, C.; Singh, A.; Kumar, A.; Liu, J.; Lan, Q. Recent advances in the electrochemical applications of Ni-based metal-organic frameworks (Ni-MOFs) and their derivatives. *Chemosphere* **2022**, *307*, 135729. [[CrossRef](#)] [[PubMed](#)]
14. Zhong, Y.; Peng, Z.; Peng, Y.; Li, B.; Pan, Y.; Ouyang, Q.; Sakiyama, H.; Muddassir, M.; Liu, J. Construction of Fe-doped ZIF-8/DOX nanocomposites for ferroptosis strategy in the treatment of breast cancer. *J. Mater. Chem. B* **2023**, *11*, 6335–6345. [[CrossRef](#)] [[PubMed](#)]
15. Zheng, M.; Chen, J.; Zhang, L.; Cheng, Y.; Lu, C.; Liu, Y.; Singh, A.; Trivedi, M.; Kumar, A.; Liu, J. Metal-organic frameworks as efficient adsorbents for drugs from wastewater. *Mater. Today Commun.* **2022**, *31*, 103514. [[CrossRef](#)]
16. Tan, J.C.; Cheetham, A.K. Mechanical properties of hybrid inorganic–organic framework materials: Establishing fundamental structure–property relationships. *Chem. Soc. Rev.* **2011**, *40*, 1059–1080. [[CrossRef](#)] [[PubMed](#)]
17. Hu, X.; Zhu, Z.; Cheng, F.; Tao, Z.; Chen, J. Micro-nano structured Ni-MOFs as high-performance cathode catalyst for rechargeable Li-O₂ batteries. *Nanoscale* **2015**, *7*, 11833–11840. [[CrossRef](#)]
18. Hu, X.; Luo, G.; Zhao, Q.; Wu, D.; Yang, T.; Wen, J.; Wang, R.; Xu, C.; Hu, N. Ru single atoms on N-doped carbon by spatial confinement and ionic substitution strategies for high-performance Li–O₂ batteries. *J. Am. Chem. Soc.* **2020**, *142*, 16776–16786. [[CrossRef](#)]
19. Banerjee, R.; Phan, A.; Wang, B.; Knobler, C.; Furukawa, H.; O’Keeffe, M.; Yaghi, O.M. High-throughput synthesis of zeolitic imidazolate frameworks and application to CO₂ capture. *Science* **2008**, *319*, 939–943. [[CrossRef](#)]
20. Park, K.S.; Ni, Z.; Côté, A.P.; Choi, J.Y.; Huang, R.; Uribe-Romo, F.J.; Chae, H.K.; O’Keeffe, M.; Yaghi, O.M. Exceptional chemical and thermal stability of zeolitic imidazolate frameworks. *Proc. Natl. Acad. Sci. USA* **2006**, *103*, 10186–10191. [[CrossRef](#)]

21. Li, Y.S.; Liang, F.Y.; Bux, H.; Feldhoff, A.; Yang, W.S.; Caro, J. Molecular sieve membrane: Supported metal-organic framework with high hydrogen selectivity. *Angew. Chem. Int. Ed.* **2010**, *49*, 548–551. [[CrossRef](#)] [[PubMed](#)]
22. Morris, W.; Leung, B.; Furukawa, H.; He, N.; Hayashi, H.; Houndonougbo, Y.; Asta, M.; Laird, B.B.; Yaghi, O.M. A combined experimental-computational investigation of carbon dioxide captures in a series of isoreticular zeolitic imidazolate frameworks. *J. Am. Chem. Soc.* **2010**, *132*, 11006–11008. [[CrossRef](#)] [[PubMed](#)]
23. Van Den Bergh, J.; Gücüyener, C.; Pidko, E.A.; Hensen, E.J., M.; Gascon, J.; Kapteijn, F. Understanding the anomalous alkane selectivity of ZIF-7 in the separation of light alkane/alkene mixtures. *Chem. Eur. J.* **2011**, *17*, 8832–8840. [[CrossRef](#)] [[PubMed](#)]
24. Zhou, X.; Zhang, H.P.; Wang, G.Y.; Yao, Z.G.; Tang, Y.R.; Zheng, S.S. Zeolitic imidazolate framework as efficient heterogeneous catalyst for the synthesis of ethyl methyl carbonate. *J. Mol. Catal. A Chem.* **2013**, *366*, 43–47. [[CrossRef](#)]
25. Phan, A.; Doonan, C.J.; Uribe-Romo, F.J.; Knobler, C.B.; Okeeffe, M.; Yaghi, O.M. Synthesis, structure, and carbon dioxide capture properties of zeolitic imidazolate frameworks. *Acc. Chem. Res.* **2010**, *43*, 58–67. [[CrossRef](#)] [[PubMed](#)]
26. Chen, Y.-Z.; Wang, C.; Wu, Z.-Y.; Xiong, Y.; Xu, Q.; Yu, S.-H.; Jiang, H.-L. From bimetallic metal-organic framework to porous carbon: High surface area and multicomponent active dopants for excellent electrocatalysis. *Adv. Mater.* **2015**, *27*, 5010–5016. [[CrossRef](#)] [[PubMed](#)]
27. Wu, X.; Meng, G.; Liu, W.; Li, T.; Yang, Q.; Sun, X.; Liu, J. Metal-organic framework-derived, Zn-doped porous carbon polyhedra with enhanced activity as bifunctional catalysts for rechargeable zinc-air battery. *Nano Res.* **2018**, *11*, 163–173. [[CrossRef](#)]
28. Harris, P.J.F. *Carbon Nanotube and Related Structures: New Materials for the 21st Century*; Cambridge University Press: Cambridge, UK, 2001.
29. Yeh, M.K.; Tai, N.H.; Liu, J.H. Mechanical behavior of phenolic-based composites reinforced with multi-walled carbon nanotubes. *Carbon* **2006**, *44*, 1–9. [[CrossRef](#)]
30. Wang, Q.; Li, C.; Bai, J.; Wang, J. Synthesis of Ag porous carbon nanofiber by electrospinning and their use as catalyst for styrene epoxidation, Synth. React. *Inorganic. Met. Nano-Metal Chem.* **2016**, *46*, 1773–1778. [[CrossRef](#)]
31. Zhao, J.; Dang, Z.; Muddassir, M.; Raza, S.; Zhong, A.; Wang, X.; Jin, J. A New Cd(II)-Based Coordination Polymer for Efficient Photocatalytic Removal of Organic Dyes. *Molecules* **2023**, *28*, 6848. [[CrossRef](#)]
32. Inagaki, M.; Yang, Y.; Kang, F. Carbon nanofibers prepared via electrospinning. *Adv. Mater.* **2012**, *24*, 2547–2566. [[CrossRef](#)] [[PubMed](#)]
33. Kim, C.; Yang, S.; Kojima, M.; Yoshida, K.; Kim, J.; Kim, A.; Endo, M. Fabrication of electrospinning-derived carbon nanofiber webs for the anode material of lithium-ion secondary batteries. *Adv. Funct. Mater.* **2006**, *16*, 2393–2397. [[CrossRef](#)]
34. Zhang, C.L.; Yu, S.H. Nanoparticles meet electrospinning: Recent advances and future prospects. *Chem. Soc. Rev.* **2014**, *43*, 4423–4448. [[CrossRef](#)] [[PubMed](#)]
35. Dalton, P.D.; Vaquette, C.; Farrugia, B.L.; Dargaville, T.R.; Brown, T.D.; Huttmacher, D.W. Electrospinning and additive manufacturing: Converging technologies. *Biomater. Sci.* **2013**, *1*, 171–185. [[CrossRef](#)] [[PubMed](#)]
36. Manawi, Y.M.; Ihsanullah Samara, A.; Al-Ansari, T.; Atieh, M.A. A review of carbon nanomaterials synthesis via the chemical vapor deposition (CVD) method. *Materials* **2018**, *11*, 822. [[CrossRef](#)] [[PubMed](#)]
37. Che, G.; Lakshmi, B.B.; Martin, C.R.; Fisher, E.R.; Ruoff, R.S. Chemical vapor deposition based synthesis of carbon nanotubes and nanofibers using a template method. *Chem. Mater.* **1998**, *10*, 260–267. [[CrossRef](#)]
38. Zhang, X.; Fan, W.; Zhao, S.; Cao, R.; Li, C. An efficient, bifunctional catalyst for lithium-oxygen batteries obtained through tuning the exterior Co²⁺/Co³⁺ ratio of CoO:X on N-doped carbon nanofibers. *Catal. Sci. Technol.* **2019**, *9*, 1998–2007. [[CrossRef](#)]
39. Tong, H.X.; Tian, X.; Wu, D.X.; Wang, C.F.; Zhang, Q.L.; Jiang, Z.H. WO₃ nanofibers on ACF by electrospun for photo-degradation of phenol solution. *J. Cent. South Univ.* **2017**, *24*, 1275–1280. [[CrossRef](#)]
40. Wang, M.X.; Guo, Z.Y.; Huang, Z.H.; Kang, F.Y. Preparation of porous carbon nanofibers with controllable pore structures for low-concentration NO removal at room temperature. *New Carbon Mater.* **2016**, *31*, 277–286. [[CrossRef](#)]
41. Aytac, Z.; Uyar, T. Applications of core-shell nanofibers. In *Drug and Biomolecules Release and Gene Therapy*; Elsevier Ltd.: Amsterdam, The Netherlands, 2018; pp. 375–404.
42. Teo, W.E.; Ramakrishna, S. A review on electrospinning design and nanofiber assemblies. *Nanotechnology* **2006**, *17*, R89–R106. [[CrossRef](#)]
43. Wang, X.; Niu, H.; Wang, X.; Lin, T. Needleless electrospinning of uniform nanofibers using spiral coil spinnerets. *J. Nanomater.* **2012**, *2012*, 785920. [[CrossRef](#)]
44. Sigmund, W.; Yuh, J.; Park, H.; Maneeratana, V.; Pyrgiotakis, G.; Daga, A.; Taylor, J.; Nino, J.C. Processing and structure relationships in electrospinning of ceramic fiber systems. *J. Am. Ceram. Soc.* **2006**, *89*, 395–407. [[CrossRef](#)]
45. Cann, J.T.M.; Li, D.; Xia, Y. Electrospinning of nanofibers with core-sheath, hollow, or porous structures. *J. Mater. Chem.* **2005**, *15*, 735–738.
46. Li, B.D.; Xia, Y. Electrospinning of nanofibers: Reinventing the Wheel? *Adv. Mater.* **2004**, *14*, 1151–1170. [[CrossRef](#)]
47. Li, D.; Wang, Y.; Xia, Y. Electrospinning of polymeric and ceramic nanofibers as uniaxially aligned arrays. *Nano Lett.* **2003**, *3*, 1167–1171. [[CrossRef](#)]
48. Li, D.; Cann, J.T.M.; Xia, Y.; Marquez, M. Electrospinning: A simple and versatile technique for producing ceramic nanofibers and nanotubes. *J. Am. Ceram. Soc.* **2006**, *89*, 1861–1869. [[CrossRef](#)]
49. Thavasi, V.; Singh, G.; Ramakrishna, S. Electrospun nanofibers in energy and environmental applications. *Energy Environ. Sci.* **2008**, *1*, 205–221. [[CrossRef](#)]

50. Xue, J.; Wu, T.; Dai, Y.; Xia, Y. Electrospinning and electrospun nanofibers: Methods, materials, and applications. *Chem. Rev.* **2019**, *119*, 5298–5415. [[CrossRef](#)]
51. Sun, B.; Long, Y.Z.; Zhang, H.D.; Li, M.M.; Duvail, J.L.; Jiang, X.Y.; Yin, H.L. Progress in Polymer Science Advances in three-dimensional nanofibres macrostructures via electrospinning. *Prog. Polym. Sci.* **2014**, *39*, 862–890. [[CrossRef](#)]
52. Tang, C.; Saquing, C.D.; Harding, J.R.; Khan, S.A.; Carolina, N. In situ cross-linking of electrospun Poly(vinyl alcohol) nanofibers. *Macromolecules* **2010**, *43*, 630–637. [[CrossRef](#)]
53. Tahir, M.S.; Lee, J.W.; Rabani, I.; Afzal, F.; Han, Y.J.; Park, H.Y.; Lee, J.; Seo, Y.S. Analysis of the porosity of ZIF-8 and ZIF-8@CNF membranes using positron annihilation lifetime spectroscopy (PALS). *J. Radioanal. Nucl.* **2023**, *332*, 3967–3975. [[CrossRef](#)]
54. Gong, X.; Luo, W.; Guo, N.; Zhang, S.; Wang, L.; Jia, D.; Ai, L.; Feng, S. Carbon nanofiber@ZIF-8 derived carbon nanosheet composites with a core-shell structure boosting capacitive deionization performance. *J. Mater. Chem. A* **2021**, *9*, 18604–18613. [[CrossRef](#)]
55. Thunberg, J.; Zacharias, S.C.; Hasani, M.; Oyetunji, O.A.; Noa FM, A.; Westman, G.; Ohrström, L. Hybrid Metal-Organic Framework-Cellulose Materials Retaining High Porosity: ZIF-8@Cellulose Nanofibrils. *Inorganics* **2021**, *9*, 84. [[CrossRef](#)]
56. Zoubir, J.; Radaa, C.; Bougdour, N.; Idlahcen, A.; Hayaoui, W.E.; Tajat, N.; Mouhri, W.E.; Nadif, I.; Qourzal, S.; Tamimi, M.; et al. A sensor based on silver nanoparticles synthesized on carbon graphite sheets for the electrochemical detection of nitrofurazone: Application: Tap water, commercial milk and human urine. *J. Indian Chem. Soc.* **2022**, *99*, 100590. [[CrossRef](#)]
57. Liu, T.; He, J.; Lu, Z.; Sun, M.; Wu, M.; Wang, X.; Jiang, Y.; Zou, P.; Rao, H.; Wang, Y. A visual electrochemiluminescence molecularly imprinted sensor with Ag⁺@UiO-66-NH₂ decorated CsPbBr₃ perovskite based on smartphone for point-of-care detection of nitrofurazone. *J. Chem. Eng.* **2022**, *429*, 132462. [[CrossRef](#)]
58. Liu, X.Y.; Huang, S.C.; Hsieh, Y.T.; Lu, S.I.; Wang, H.H.; Wang, C.C.; Chuang, Y.C. Detection of nitrofurazone with metal organic frameworks and reduced graphene oxide composites: Insights from molecular dynamics simulations. *Microchim. Acta* **2023**, *190*, 246. [[CrossRef](#)]
59. Wang, H.; Pei, F.; Liu, C.; Ni, Y.; Xia, M.; Feng, S.; Hao, Q.; Yang, T.; Lei, W. Efficient detection for nitrofurazone based on novel Ag₂S QDs/g-C₃N₄ fluorescent probe. *Spectrochim. Acta A* **2022**, *269*, 120727. [[CrossRef](#)]
60. Yeh, M.Y.; Liu, Y.R.; Huang, T.H.; Chen, Y.H.; Hsieh, Y.T. Electrochemical Sensing of nitrofurazone and semicarbazide on an Au-Ag film fabricating from a deep eutectic solvent. *J. Electrochem. Soc.* **2022**, *169*, 107502. [[CrossRef](#)]
61. Lu, Y.S.; Pan, W.Y.; Hung, T.C.; Hsieh, Y.T. Electrodeposition of silver in a ternary deep eutectic solvent and the electrochemical sensing ability of the Ag-modified electrode for nitrofurazone. *Langmuir* **2020**, *36*, 11358–11365. [[CrossRef](#)]
62. Baby, J.N.; Sriram, B.; Wang, S.F.; George, M. Versatile deep eutectic solvent assisted synthesis of ZnB₂O₄ (B = Al, Co, Cr spinels: The effect of B site variants for comparing the bifunctional electrochemical sensing application. *J. Chem. Eng.* **2022**, *435*, 134136. [[CrossRef](#)]

Disclaimer/Publisher's Note: The statements, opinions and data contained in all publications are solely those of the individual author(s) and contributor(s) and not of MDPI and/or the editor(s). MDPI and/or the editor(s) disclaim responsibility for any injury to people or property resulting from any ideas, methods, instructions or products referred to in the content.